The Generation and Propagation of the Human Alpha Rhythm

Milan Halgren, Orrin Devinsky, Werner K. Doyle, Hélène Bastuji, Marc Rey, Rachel Mak-McCully, Patrick Chauvel, István Ulbert, Dániel Fabó, Lorand Erőss, Lucia Wittner, Gary Heit, Emad Eskandar, Arnold Mandell, Sydney S. Cash

Contact: mhalgren@mgh.harvard.edu

Introduction

The alpha rhythm (7-13 Hz) is the longest studied brain oscillation and has been theorized to play a key role in cognition. Still, substantial uncertainty remains over its physiology. In this study, we used micro and macro electrodes in patients undergoing surgery for epilepsy to measure the intracortical and thalamic generators of the human alpha rhythm. We first found that alpha propagates from higher-order anterosuperior cortex towards the lower-order occipital poles, consistent with alpha effecting top-down processing. This cortical alpha drives thalamic alpha, reversing prevailing theories of a thalamic alpha pacemaker. Finally, alpha is dominated by currents and firing in supragranular cortex, contravening the popular conception of alpha as an infragranular rhythm. Together, these results demonstrate that the alpha rhythm reflects short-range supragranular feedback which propagates from higher-order to lower order cortex and cortex to thalamus. These physiological insights explain how alpha could mediate feedback throughout the thalamocortical system.

Alpha oscillations (7-13 Hz)[1,2] are the most salient EEG event during wakefulness and may be fundamental for top-down cognitive processes such as attention[3], perception[4,5], functional inhibition[6] and working memory[7]. However, the underlying neural structure(s) and circuits which generate alpha are intensely controversial. Studies have pointed to the thalamus as the primary alpha pacemaker, with the classic posterior alpha rhythm driven by the pulvinar and/or lateral geniculate nucleus (LGN)[3,8,9]. Within the cortex, it's widely assumed that alpha originates from infragranular layers driven by layer V pyramidal cells[10–12]. Despite the prevalence of these hypotheses, the studies used to support them are not definitive; previous electrophysiological literature have either used a distant reference susceptible to volume conduction[3,10,12], were performed in vitro[11] or relied on imprecise extracranial recordings[13]. Crucially, these hypotheses have not been directly tested via invasive recordings in humans. We therefore analyzed focal micro and macro electrode recordings from human neocortex and thalamus in surgical epilepsy patients to characterize alpha's generation during quiet wakefulness.

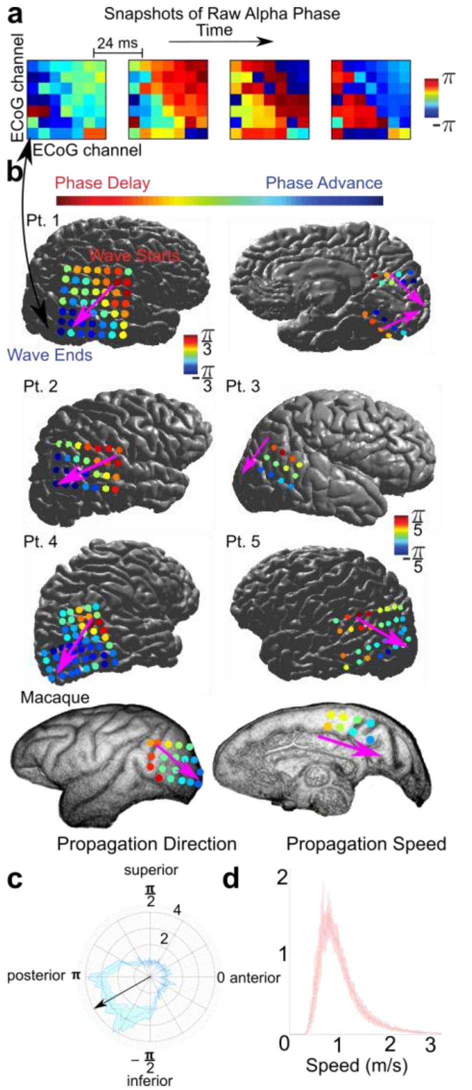

Fig. 1: Alpha Propagates from Anterosuperior to Posteroinferior Cortex

a Alpha-phase anapshots from Pt. 1 demonstrates propagation from the grid's top-right (anterosuperior) to bottom-left corner (posteroinferior). **b** Average circular distance of each contact's alpha-phase from the spatial mean phase during eye-closure. In all patients, alpha propagates towards posteroinferior areas. Overlaid arrow is the direction of the grid's average phase gradient. Color runs from $\pm\frac{\pi}{3}$ in Pts. 1, 2, 5 and macaque, and from $\pm\frac{\pi}{5}$ in Pts. 3-4. **c** Average probability distribution of travelling wave directions across time, with each grid re-aligned such that the bottom left contact is the most posteroinferior (±S.E.M. across patients). **d** Average probability distribution of travelling wave speeds (±S.E.M. across patients).

Alpha is a Travelling Wave from Anterosuperior to Inferoposterior Regions.

We analyzed electrocorticography (ECoG) recordings of alpha oscillations in the occipital, posterior temporal, and parietal cortices of 5 patients (3 of whom engaged in an eye closure task) (**Extended Data Fig. 1, Extended Data Table 1**). Strikingly, alpha oscillations propagated as travelling waves from anterosuperior cortex towards posteroinferior areas (**Fig. 1a,b,d**). This propagation was visualized by finding the time-averaged alpha-band phase difference between each channel and the mean alpha-band phase across all contacts, yielding a positive difference if the channel was lagging the oscillation (propagating from) and negative if it was leading (propagating to) (**Extended Data Fig. 2**)[14]. We confirmed that alpha had a consistent propagation direction in each patient by finding the direction of the average spatial phase gradient across the grid of electrodes at each time point, and then determining if the distribution of gradient directions throughout the grid was non-uniform[15] ($p \leq 10^{-200}$ across patients, Rayleigh Test) (**Fig. 1d, Extended Data Fig. 3, Methods**). Estimated median speeds of these waves (derived from the phase-gradient) were just under 1 m/s (median speed across patients: .9134 +- .1563 m/s). (**Extended Data Fig. 4, Methods**). Open-source ECoG recordings in a healthy macaque during eye closure demonstrated a highly similar propagation direction and speed[16] (**Fig. 1b**).

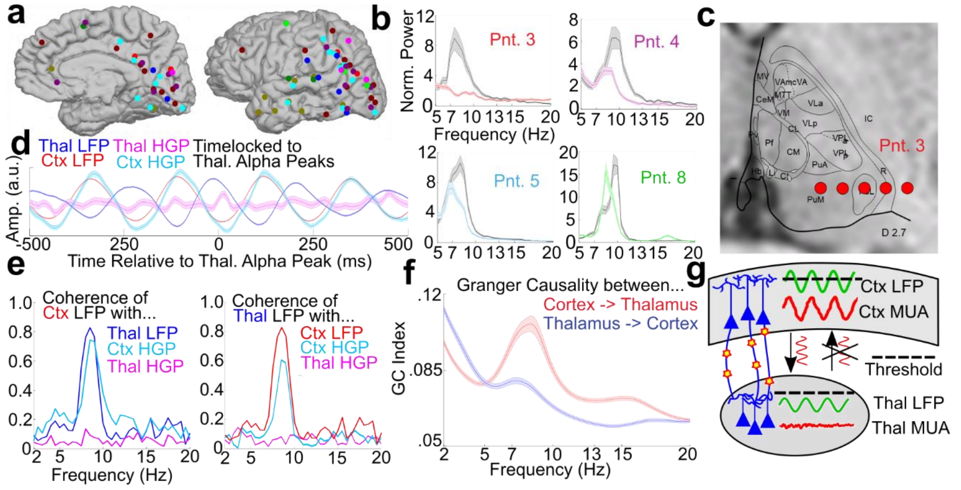

Fig. 2: Cortical Alpha Drives Thalamic Alpha a Cortical implant locations in all patients displayed on Pt. 3's brain for reference. Each color signifies a different patient. **b** Power spectra of the thalamic (color) and cortical (grey) channel with the greatest alpha power. **c** Contact locations in Pt. 3 on thalamic outline overlaid on MRI. **d** Cortical and thalamic LFP and HGP from representative channels locked to peaks in thalamic alpha LFP – note that cortical, but not thalamic, firing is phasic with thalamic LFP. **e** Coherence spectra of thalamic and cortical LFP with thalamic and cortical HGP and LFP from the same channel pair in **d**; the coherence of cortical (but not thalamic) HGP with thalamic LFP indicates cortical generation of thalamic alpha activity. **f** Granger Causality spectra averaged over all thalamocortical contact pairs corticothalamic causality shows a strong alpha peak. **g** Schematic summarizing thalamocortical findings; cortical (but not thalamic) HGP (red) is synchronous with thalamic and cortical alpha LFP (green), indicating that the spiking of cortical neurons drives alpha.

Corticothalamic Generation

To determine if the thalamus coordinated these travelling alpha waves, we utilized bipolar local-field-potential (LFP) depth recordings (n=9) obtained simultaneously from cortex and the pulvinar (**Fig. 2b**), a thalamic nucleus which projects broadly to posterior cortical regions[17] and postulated to drive cortical alpha[3,18]. Surprisingly, power spectra from cortical contacts had alpha-band peaks more frequently (63.4%, 78/123) than thalamic ones (34.6%, 9/26) (**Fig. 2b, Extended Data Fig. 5, Methods**). To determine whether cortical or thalamic activity was driving these rhythms, we extracted high-gamma-power (HGP), a proxy for neural firing, in both structures (n=5; 70-120 Hz in Pts. 1-3, 70-190 Hz in Pts. 8-9, Pts. 4-7 were excluded due to low sampling rates). If a given structure is generating alpha oscillations, its HGP should be synchronous with its alpha-band LFP. This synchrony was assessed using two methods; Tort's Modulation Index (MI)[19] and the coherence between the time-domain LFP and HGP [20] (**Fig. 2e, Extended Data Fig. 6**). Notably, thalamic alpha was rarely coherent with its own firing (Coherence: 0/42 intrathalamic contact pairs, MI: 3/42, $p < .05$ Bonferroni Corrected within patients); Instead, thalamic alpha rhythms were predominantly synchronous with cortical HGP (Coherence and MI: 9/15) (**Fig. 2e**), consistent with cortical generation. To confirm that thalamic alpha was cortically driven, we measured Granger Causality spectra between all pairs of cortical and thalamic contacts[21] (**Fig. 2f**). Corticothalamic causality in the alpha band was found to be significantly greater than thalamocortical causation for almost every thalamocortical channel pair (across all patients) with a significant difference between thalamocortical and corticothalamic causation ($p \leq .01$ for each channel pair, Wilcoxon Signed Rank Test, Bonferroni Corrected within subjects; 143/163 (87.73%) pairs with greater corticothalamic than thalamocortical causality; $p < 1.83 \ast 10^{-24}$ across all significantly different channel pairs, Binomial Test).

Laminar Generation of Alpha Activity To determine which cortical layers generate the alpha rhythm, we utilized laminar microelectrodes[22] to record current-source-density (CSD, n=3) and HGP (n=2) across gray matter layers[22]. In all patients, alpha-band currents were strongest within superficial cortical layers (Pt. 1: $p<2.27 \ast 10^{-25}$, Pt. 2: $p<1.9 \ast 10^{-22}$, Pt. 3: $p<1.66 \ast 10^{-5}$; largest p-values of Wilcoxon Sign Rank comparing mean alpha power in supragranular versus granular and infragranular channels across epochs, Bonferroni corrected) (**Fig. 3d,g, Extended Data Fig. 7**). Averaging HGP on alpha current sinks as well as measuring Tort's MI between alpha CSD and HGP (**Fig. 3e, f**) reveals that alpha-band firing is located in layers I-III, implying that supragranular pyramidal cells are the principal generators of the human alpha rhythm (Multiunit activity yielded similar results; see **Extended Data Fig. 9**). Furthermore, this supragranular firing was maximal during very superficial sinks and minimal during superficial sources, consistent with active synaptic and/or voltage gated currents in layers I/II. This sink-source configuration extends the previous intra and extracranial finding[23,24] that firing is maximal during the surface-negative peak of the alpha-rhythm by showing that this firing reflects increased supragranular activity caused by very superficial current sinks.

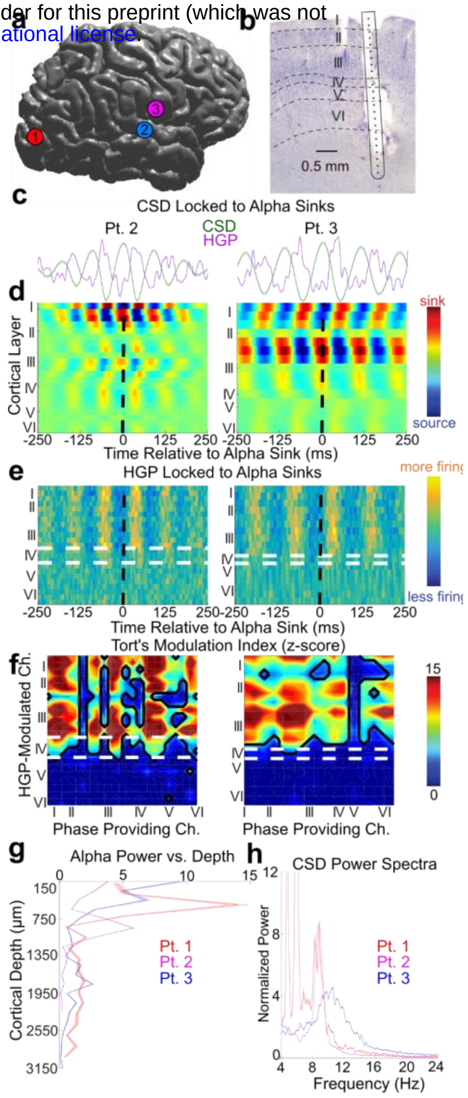

Fig. 3: Alpha is Generated in Supragranular Cortex a Locations of each microelectrode probe on the brain of Pt. 2. **b** Schematic of Pt. 3's laminar array with co-histology (Nissl stain). **c** Average single-channel CSD and HGP waveforms of a single channel on same time-axes as **d** (±S.E.M. across alpha sinks). **d** CSD and **e** HGP averaged on current sinks in channels 3 and 6 in Pts. 2 and 3, respectively; white and black dashed lines indicate layer IV boundaries and the time of the alpha-sink, respectively. **f** Z-score of the MI between alpha phase and HGP across all channels. **g** Average alpha power throughout the cortical depth. (±S.E.M. across epochs). **h** Power spectra of the channel with greatest alpha power in each subject. (±S.E.M. across epochs).

Discussion

Our results demonstrate that alpha is uniquely poised to mediate feedback processing within and across brain regions and structures. These findings build on non-human-primate single site recordings that found alpha spread from V2 to V1[10] and human travelling wave studies with inconsistent propagation directions[23] by demonstrating that the posterior alpha rhythm propagates as a travelling wave across widespread regions towards the occipital pole. The anatomical propagation of alpha waves from anterosuperior to posteroinferior cortex implies a functional progression from higher-order to lower-order visual areas, matching alpha's putative role as a feedback rhythm[10]. This might serve as a mechanism to internally scan the attentional field, tag distinct visual features with different phases[25], or facilitate plasticity between upstream and downstream areas[26,27].

Simultaneous recordings from human cortex and pulvinar revealed that thalamic alpha was less common than cortical alpha, synchronous with cortical (but not thalamic) firing and was Granger-Caused by cortical alpha. Although posterior cortical alpha might be driven by the LGN and therefore still have a thalamic origin, the LGN is an unlikely cortical pacemaker as its major projections are limited to striate and circumstriate cortex[17] and we found that alpha oscillations propagate towards (and not from) the occipital pole. Because the LGN and pulvinar are the two thalamic nuclei with the most robust projections to posterior cortex capable of driving visual alpha, these findings are most consistent with a cortical alpha pacemaker during quiet wakefulness. Although this appears to contradict animal studies in which the pulvinar drove cortical alpha, it's consonant with findings that the cortex can still generate alpha in vitro[11] and actually shows increased alpha-band power when the pulvinar is inactivated[18], as well as alpha coherence within the cortex exceeding thalamocortical alpha coherence [28]. These findings might be reconciled with other studies supporting thalamic alpha generators[3,29] if there are separable thalamic and cortical alpha generators, or if the pulvinar enables cortical alpha activity with tonic (non-rhythmic) excitation/inhibition without being a direct pacemaker[30].

Laminar microelectrode recordings revealed that both alpha currents and firing are strongest in superficial cortex, indicating that supragranular pyramidal neurons are the primary drivers of the human alpha rhythm. While most models posit that layer V (infragranular) pyramidal cells drive alpha[10,11,31], these are based mostly on monopolar LFP recordings[24] which (unlike CSD) are prone to volume conduction from deep sources. However, infragranular interneurons might still play a role in alpha generation via rhythmic inhibition of supragranular pyramidal cells. A weaker modulation of granular firing might indicate that alpha blocks layer IV feedforward input by coupling it to endogenous supragranular oscillations; this provides a laminar circuit for dynamically deafferenting cortical areas and enacting alpha's well characterized role in functional inhibition[6]. Alpha's laminar physiology was highly similar in all penetrations despite our recordings being made from occipital, temporal and parietal cortices; this supports alpha reflecting a common function subserved by similar physiology throughout the cortex[24]. The finding that alpha oscillations are driven by layer I/II currents (postsynaptic) and layer I-III firing (presynaptic) matches the canonical laminar pathway for short-range feedback, originating in layers II/III and projecting to layers I-III[32]. This laminar circuit is also the most likely intracortical mechanism to drive the alpha travelling waves we measured using ECoG, which propagate continuously from high to low order cortex (i.e. not in the saltatory manner that would be expected if mediated by long-

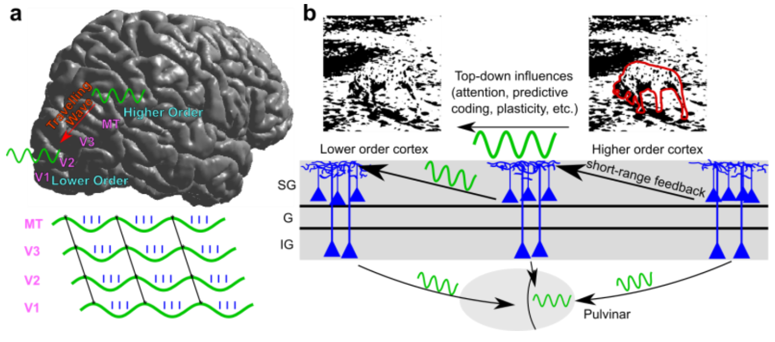

Fig. 4: **Alpha acts as a feedback rhythm a** Alpha propagates as a travelling wave from higher order towards lower order cortical areas. **b** Alpha is generated by supragranular cortex and carries top-down information via short-range feedback connections to constrain lower-level processing. Cortical alpha in layer VI also drives alpha activity within the pulvinar.

range feedback). Furthermore, measured propagation speeds were generally < 1 m/s, closer to previously measured conduction velocities of intracortical fibers (as opposed to corticocortical white-matter tracts)[33]. These constitute converging lines of evidence for cortical alpha reflecting short-range intracortical feedback within superficial layers.

Alpha's top-down propagation as a travelling wave (both from higher to lower order cortex and from cortex to thalamus) indicates that it could fine-tune the weights of feedback synapses via spike-timing-dependent-plasticity (STDP), similar to how other travelling waves mediate STDP by compensating for axonal conduction delays[34]. Thus, alpha could play a key role in memory consolidation during wakefulness, consistent with strong alpha in regions which are 'offline'[6]. During active perception, corticothalamic alpha might functionally inhibit the thalamus to gate feedforward processing and suppress irrelevant neural assemblies akin to its putative role within the cortex[6], as low-frequency corticothalamic activity inhibits thalamic firing[35]. Cortically, alpha's generation by supragranular synaptic and unit activity is consistent with an integrative function due to the termination of widespread associative and feedback connections in superficial layers[32] as well as the modulatory role of layer I/II apical dendrites[36]. A supragranular origin for the alpha rhythm is also in accord with its putative role in neural inhibition[37], as layers I/II contain a dense interneuronal network which strongly inhibits the apical dendrites of excitatory cells throughout the cortical column[38,39]. This short-range feedback inhibition would allow higher-order cortex to modulate the gain of lower order areas throughout visual cortex, providing a laminar circuit for top-down processes such as attention. It also comports with a predictive coding framework in which supragranular cells at each level of the cortical hierarchy use alpha to sequentially transmit sensory predictions down to, and/or suppress residual prediction errors from, the area hierarchically below it[40,41]. In all, we find that alpha acts within the nervous system by propagating from cortex to thalamus and higher-order to lower-order cortex, likely via short-range supragranular feedback projections. These intracortical and corticothalamic dynamics could allow alpha to sculpt activity throughout the neural hierarchy.

References:

1. Berger, H. Das Elektrenkephalogramm des Menschen. *Naturwissenschaften* **23,** 121–124 (1935).
2. Haegens, S., Cousijn, H., Wallis, G., Harrison, P. J. & Nobre, A. C. Inter- and intra-individual variability in alpha peak frequency. *Neuroimage* **92,** 46–55 (2014).
3. Saalmann, Y. B., Pinsk, M. A., Wang, L., Li, X. & Kastner, S. The Pulvinar Regulates Information Transmission Between Cortical Areas Based on Attention Demands. *Science (80-.).* **337,** 753–756 (2012).
4. Samaha, J. & Postle, B. R. The Speed of Alpha-Band Oscillations Predicts the Temporal Resolution of Visual Perception. *Curr. Biol.* **25,** 2985–2990 (2015).
5. Busch, N. A., Dubois, J. & VanRullen, R. The Phase of Ongoing EEG Oscillations Predicts Visual Perception. *J. Neurosci.* **29,** 7869–7876 (2009).
6. Jensen, O. & Mazaheri, A. Shaping functional architecture by oscillatory alpha activity: gating by inhibition. *Front. Hum. Neurosci.* **4,** 186 (2010).

7. Jensen, O. Oscillations in the Alpha Band (9-12 Hz) Increase with Memory Load during Retention in a Short-term Memory Task. *Cereb. Cortex* **12,** 877–882 (2002).
8. Lorincz, M. L., Kékesi, K. a., Juhász, G., Crunelli, V. & Hughes, S. W. Temporal Framing of Thalamic Relay-Mode Firing by Phasic Inhibition during the Alpha Rhythm. *Neuron* **63,** 683–696 (2009).
9. Hughes, S. W. *et al.* Thalamic gap junctions control local neuronal synchrony and influence macroscopic oscillation amplitude during EEG alpha rhythms. *Front. Psychol.* **2,** (2011).
10. van Kerkoerle, T. *et al.* Alpha and gamma oscillations characterize feedback and feedforward processing in monkey visual cortex. *Proc. Natl. Acad. Sci.* **111,** 14332–14341 (2014).
11. Silva, L., Amitai, Y. & Connors, B. Intrinsic oscillations of neocortex generated by layer 5 pyramidal neurons. *Science (80-.).* **251,** 432–435 (1991).
12. Buffalo, E. a, Fries, P., Landman, R., Buschman, T. J. & Desimone, R. Laminar differences in gamma and alpha coherence in the ventral stream. *Proc. Natl. Acad. Sci. U. S. A.* **108,** 11262–7 (2011).
13. Roux, F., Wibral, M., Singer, W., Aru, J. & Uhlhaas, P. J. The Phase of Thalamic Alpha Activity Modulates Cortical Gamma-Band Activity: Evidence from Resting-State MEG Recordings. *J. Neurosci.* **33,** 17827–17835 (2013).
14. Zhang, H. & Jacobs, J. Traveling Theta Waves in the Human Hippocampus. *J. Neurosci.* **35,** 12477–12487 (2015).
15. Rubino, D., Robbins, K. A. & Hatsopoulos, N. G. Propagating waves mediate information transfer in the motor cortex. *Nat. Neurosci.* **9,** 1549–1557 (2006).
16. Nagasaka, Y., Shimoda, K. & Fujii, N. Multidimensional recording (MDR) and data sharing: An ecological open research and educational platform for neuroscience. *PLoS One* **6,** (2011).
17. Nieuwenhuys, R., Voogd, J. & van Huijzen, C. *The Human Central Nervous System*. (Springer Berlin Heidelberg, 2008). doi:10.1007/978-3-540-34686-9
18. Zhou, H., Schafer, R. J. & Desimone, R. Pulvinar-Cortex Interactions in Vision and Attention. *Neuron* **89,** 209–220 (2016).
19. Tort, A. B. L., Komorowski, R., Eichenbaum, H. & Kopell, N. Measuring Phase-Amplitude Coupling Between Neuronal Oscillations of Different Frequencies. *J. Neurophysiol.* **104,** 1195–1210 (2010).
20. Colgin, L. L. *et al.* Frequency of gamma oscillations routes flow of information in the hippocampus. *Nature* **462,** 353–357 (2009).
21. Barnett, L. & Seth, A. K. The MVGC multivariate Granger causality toolbox: A new approach to Granger-causal inference. *J. Neurosci. Methods* **223,** 50–68 (2014).
22. Ulbert, I., Halgren, E., Heit, G. & Karmos, G. Multiple microelectrode-recording system for human intracortical applications. *J. Neurosci. Methods* **106,** 69–79 (2001).

23. Bahramisharif, A. *et al.* Propagating neocortical gamma bursts are coordinated by traveling alpha waves. *J. Neurosci.* **33,** 18849–18854 (2013).

24. Haegens, S. *et al.* Laminar Profile and Physiology of the α Rhythm in Primary Visual, Auditory, and Somatosensory Regions of Neocortex. *J. Neurosci.* **35,** 14341–52 (2015).

25. Ermentrout, G. B. & Kleinfeld, D. Traveling Electrical Waves in Cortex. *Neuron* **29,** 33–44 (2001).

26. Bennett, J. E. M. & Bair, W. Refinement and Pattern Formation in Neural Circuits by the Interaction of Traveling Waves with Spike-Timing Dependent Plasticity. *PLOS Comput. Biol.* **11,** e1004422 (2015).

27. Han, F., Caporale, N. & Dan, Y. Reverberation of Recent Visual Experience in Spontaneous Cortical Waves. *Neuron* **60,** 321–327 (2008).

28. Lopes da Silva, F. H., van Lierop, T. H. M. T., Schrijer, C. F. & Storm van Leeuwen, W. Organization of thalamic and cortical alpha rhythms: Spectra and coherences. *Electroencephalogr. Clin. Neurophysiol.* **35,** 627–639 (1973).

29. Hughes, S. W. & Crunelli, V. Thalamic mechanisms of EEG alpha rhythms and their pathological implications. *Neuroscientist* **11,** 357–372 (2005).

30. Quax, S., Jensen, O. & Tiesinga, P. Top-down control of cortical gamma-band communication via pulvinar induced phase shifts in the alpha rhythm. *PLoS Comput. Biol.* **13,** (2017).

31. Dougherty, K., Cox, M. A., Ninomiya, T., Leopold, D. A. & Maier, A. Ongoing Alpha Activity in V1 Regulates Visually Driven Spiking Responses. *Cereb. Cortex* bhv304 (2015). doi:10.1093/cercor/bhv304

32. Markov, N. T. *et al.* Anatomy of hierarchy: Feedforward and feedback pathways in macaque visual cortex. *J. Comp. Neurol.* **522,** 225–259 (2014).

33. Girard, P., Hupe, J. M. & Bullier, J. Feedforward and feedback connections between areas V1 and V2 of the monkey have similar rapid conduction velocities. *J Neurophysiol* **85,** 1328–31. (2001).

34. Muller, L. *et al.* Rotating waves during human sleep spindles organize global patterns of activity that repeat precisely through the night. *Elife* **5,** (2016).

35. Crandall, S. R., Cruikshank, S. J. & Connors, B. W. A Corticothalamic Switch: Controlling the Thalamus with Dynamic Synapses. *Neuron* **86,** 768–782 (2015).

36. Larkum, M. A cellular mechanism for cortical associations: an organizing principle for the cerebral cortex. *Trends Neurosci.* **36,** 141–151 (2013).

37. Haegens, S., Nacher, V., Luna, R., Romo, R. & Jensen, O. Oscillations in the monkey sensorimotor network influence discrimination performance by rhythmical inhibition of neuronal spiking. *Proc. Natl. Acad. Sci.* **108,** 19377–19382 (2011).

38. Chu, Z., Galarreta, M. & Hestrin, S. Synaptic Interactions of Late-Spiking Neocortical Neurons in Layer 1. *J. Neurosci.* **23,** 96–102 (2003).

39. Meyer, H. S. *et al.* Inhibitory interneurons in a cortical column form hot zones of inhibition in layers 2 and 5A. *Proc. Natl. Acad. Sci.* **108,** 16807–16812 (2011).
40. Bastos, A. M. *et al.* Canonical Microcircuits for Predictive Coding. *Neuron* **76,** 695–711 (2012).
41. Clark, A. *et al.* Whatever next? Predictive brains, situated agents, and the future of cognitive science. *Behav. Brain Sci.* **36,** 181–204 (2013).
42. Berens, P. CircStat: A MATLAB toolbox for circular statistics. *J. Stat. Softw.* **31,** 1–21 (2009).
43. Oostenveld, R., Fries, P., Maris, E. & Schoffelen, J.-M. FieldTrip: Open Source Software for Advanced Analysis of MEG, EEG, and Invasive Electrophysiological Data. *Comput. Intell. Neurosci.* **2011,** 1–9 (2011).
44. Rosenberg, J. R., Amjad, A. M., Breeze, P., Brillinger, D. R. & Halliday, D. M. The Fourier approach to the identification of functional coupling between neuronal spike trains. *Prog. Biophys. Mol. Biol.* **53,** 1–31 (1989).
45. Cohen, M. X. *Analyzing Neural Time Series Data: Theory and Practice. MIT Press* (2014). doi:10.1017/CBO9781107415324.004
46. D'Errico, J. inpaint_nans. (2012).
47. Dale, A. M., Fischl, B. & Sereno, M. I. Cortical Surface-Based Analysis: I. Segmentation and Surface Reconstruction. *Neuroimage* **9,** 179–194 (1999).
48. Yang, A. I. *et al.* Localization of dense intracranial electrode arrays using magnetic resonance imaging. *Neuroimage* **63,** 157–165 (2012).
49. Dykstra, A. R. *et al.* Individualized localization and cortical surface-based registration of intracranial electrodes. *Neuroimage* **59,** 3563–3570 (2012).
50. Cohen, M. X. Fluctuations in Oscillation Frequency Control Spike Timing. *J. Neurosci.* **34,** 8988–8998 (2014).
51. Talairach, J. *et al.* Surgical therapy for frontal epilepsies. *Adv. Neurol.* **57,** 707–32 (1992).
52. Morel, A., Magnin, M. & Jeanmonod, D. Multiarchitectonic and stereotactic atlas of the human thalamus. *J. Comp. Neurol.* **387,** 588–630 (1997).
53. Mak-McCully, R. a *et al.* Distribution, Amplitude, Incidence, Co-Occurrence, and Propagation of Human K-Complexes in Focal Transcortical Recordings. *eNeuro* **2,** 3 (2015).
54. Rechtschaffen, A. & Kales, A. A manual of standardised terminology, techniques, and scoring system for sleep stages of human subjects. *Los Angelos UCLA Brain Inf. Serv.* . **2115,** 2115 (1968).
55. Yoder, N. Peakfinder. (2011).
56. Ulbert, I., Karmos, G., Heit, G. & Halgren, E. Early discrimination of coherent versus incoherent motion by multiunit and synaptic activity in human putative MT+. *Hum. Brain Mapp.* **13,** 226–238 (2001).

57. Nicholson, C. & Freeman, J. A. Theory of current source-density analysis and determination of conductivity tensor for anuran cerebellum. *J. Neurophysiol.* **38,** 356–368 (1975).

58. Vaknin, G., DiScenna, P. G. & Teyler, T. J. A method for calculating current source density (CSD) analysis without resorting to recording sites outside the sampling volume. *J. Neurosci. Methods* **24,** 131–135 (1988).

Methods

Patients

Implantations were performed on patients with pharmacologically-resistant epilepsy undergoing surgery to locate and resect seizure foci. Seventeen patients (10 female, ages 15-50) were informed of potential risks and told that they had no obligation to participate in the study, as well as being informed that their decision to participate wouldn't affect their clinical care. Experiments were made with fully informed consent as specified by the Declaration of Helsinki and approved by local institutional review boards. These boards included the Partners Health Care IRB, NYU Medical Center IRB, Stanford IRB, and the Hungarian Medical Scientific Council. All decisions concerning macroelectrode placement were made solely on a clinical basis, whereas laminar microelectrodes were inserted into cortex likely to be resected.

Numbering for patients was started anew for each measurement modality, and no patients had more than one kind of electrode (ECoG, SEEG or laminar) analyzed.

All recordings other than those during our eye-closure task were made of spontaneous activity during quiet wakefulness, in which the patient was not engaged in a cognitive task.

General Analysis Procedures

Recordings were analyzed using custom MATLAB scripts with the CircStat[42] and Fieldtrip[43] Toolboxes.

Prior to further analysis, the raw data was visually inspected for artifacts due to machine noise, patient movement, or epileptiform activity. Epochs containing these artifacts (as judged by an expert neurologist) were removed prior to further analysis.

Unless otherwise specified, all analyses of alpha-band effects refer to the 7-13 Hz band. Error bars correspond to the standard error of the mean (S.E.M.).

Power and cross-spectral densities were found via the multi-taper method. This was performed by applying a Hanning taper and then taking the Fourier Transform of the zero-meaned data.

Coherence (**Fig. 2e, Extended Data Fig. 4a**) was calculated using the ft_connectivity function, which defines the coherence between mean subtracted time series x and y as $Coh(x,y) = \left| \frac{S_{xy}}{S_{xx}S_{yy}} \right|$, where S_{xy} is the cross-spectral density between x and y and S_{xx} is the autospectral density of x[44]. In order to quantify alpha-high gamma phase-amplitude-coupling, we measured the coherence between the broadband LFP and Hilbert amplitude of the high-gamma filtered data. To determine the statistical significance of coherence between all channel pairs, we generated a reference distribution of coherence values under the null hypothesis of no temporal relationship between each pair of time-series[45]. This was accomplished by shuffling the temporal order of 2-second epochs for each channel 200 times, and then recalculating the coherencies between all channels. To calculate the significance of coherencies in the alpha-band, we summed the coherence between 7-13 Hz for each permutation, and then used the mean and standard deviation of this reference distribution of alpha coherencies to determine the z-score of the real summed coherence between 7-13 Hz. Coherencies were deemed significant at $p < .05$, Bonferroni corrected within subjects (or $p < .05$ / (number of channel pairs / 2) for each subject).

To derive alpha and high-gamma amplitude as well as alpha phase, we used the Hilbert Transform. First, data was filtered using a two-pass fourth-order IIR Butterworth Filter. Then, the analytic signal $z(t)$ was found by applying the Hilbert Transform to the filtered signal of each channel. The phase series $\phi(t)$ was found by taking the angle of the analytic signal, and the amplitude $A(t)$ of every channel was found by taking the real component of the analytic signal.

To determine the effects of alpha rhythms on neural firing, we used Tort's Modulation Index[19] (**Fig. 3f, Extended Data Fig. 6b**) with a non-parametric trial shuffling procedure to assess significance. First, we applied the Hilbert Transform (see above) to derive amplitude series $A(t)$ and phase series $\phi(t)$. $\phi(t)$ was then reordered from $-\pi$ to $+\pi$, and $A(t)$ for every other channel and frequency was reordered using the same permutation vector. Amplitude was then averaged within 36 bins of phase (i.e. 10 degrees) and normalized by the sum over bins, yielding ϕ. The modulation index (MI) was then calculated as $MI(\phi) = \left|\frac{D_{kl}(\phi, u)}{\log(36)}\right|$ for each channel and frequency pair, where D_{kl} is the Kullback-Leibler divergence, u is the uniform distribution (i.e. no relationship between amplitude and phase) and log(36) is the natural logarithm of the number of phase bins[19]. D_{kl} was computed as log(36) – H(P), where H(P) was the distribution's Shannon's Entropy.

Statistical significance of MI values was determined similarly to coherence (a reference distribution under the null hypothesis of a random relationship between amplitude and phase was formed, the MI was calculated for each shuffled data set and the mean and variance of these null hypothesis derived MIs at each channel and frequency were used to determine the z-score of the actual MIs at each channel and modulating/modulated frequency pair). Instead of shuffling the temporal order of two second epochs to create surrogate datasets we iteratively split the phase series into two epochs 200 times, the split point being 20-80% through the length of the data, and swapped their order.

Travelling Waves

We utilized 4.54±.87 minutes (mean ± standard deviation) of ECoG recordings made for clinical purposes. These arrays had 2-mm contact diameters and 1-cm intercontact spacing, and were referenced to 1-4 inactive electrodes placed outside of the dura facing the skull. In Patients 1, 3 and 4, patients were instructed to open and close their eyes with an audial cue at 15 second intervals using Presentation software (Neurobehavioral Systems, Albany, CA, USA). We only utilized activity during eye-closure in these patients (except for **Extended Data Fig. 4**). In Patients 4-5 (who didn't participate in the eye-closure task), we analyzed spontaneous activity during quiet wakefulness. We also analyzed 16.5 minutes of open-source ECoG recordings made from a macaque monkey during an eye closure task. Eyes were closed via a sleep mask for 10 minutes, and the sleep mask was then removed for 10 minutes of data. The Macaque was included in group statistics with other patients due to its high similarity with human activity (**Extended Data Fig. 4**). Further details concerning the macaque recording can be found at Neurotycho.org[16]. Time-domain data in Pts. 1 and 5 were spatially interpolated in missing channels (using inpaint_nans[46]) prior to further analysis.

To localize contacts to the pial surface, we aligned a pre-operative MRI with a structural MRI or CT. These contact locations were then displayed on the reconstructed cortical surface, created using Freesurfer[47], of each individual patient (**Fig. 1b, 3a, Extended Data Fig. 3**) [48,49].

We first used a two-pass third-order zero-phase shift Butterworth Filter between 7-13 Hz to extract alpha-band activity. The Hilbert Transform was then applied to find both the amplitude and phase of ongoing alpha activity. Consistent with laminar and SEEG analyses, we then selected artifact-free three second epochs with the highest 20% of average alpha-band amplitude across array channels to analyze further.

To visualize the spatial progression of alpha oscillations across the array, we found the circular difference between the mean phase across all contacts and each individual contact at each point in time (**Extended Data Fig. 1**). This yields a distribution of differences of each contact's phase from the grid's mean phase across all time-points. We then found the circular mean of this difference – if a contact is leading an oscillation, it will have a positive circular distance with respect to the grid's spatial mean phase. If a contact is lagging, it will have a negative phase difference with the grid's average phase. **Fig. 1b** was then generated by finding the mean circular distance between each contacts phase and the grid's mean phase at each timepoint, or the average advance/delay of a given contact. This method allows one to measure travelling waves oblique to the grid's implantation and sidestep the selection of a potentially biasing reference contact. This analysis was performed separately for strips and grids as well as strips >2 cm apart, as the large cortical distances between them would make phase differences difficult to interpret.

We then wished to measure the directionality of these travelling waves. To do this we employed the phase gradient ∇, found by using MATLAB's gradient function (but with subtractions replaced with circular distances). To prove that there was a consistent directionality of propagation across time, at each time-point we found the median direction of the gradient throughout the grid. Using Rayleigh's test for non-uniformity demonstrated that each patient had a significant propagation direction (**Extended Data Fig. 3**). To generate **Fig. 1d**, we binned the travelling wave directions across time into 100 bins normalized within patients (i.e. divided the count of each bin by the total number of time-points), and then averaged across patients (with the error bar being the S.E.M. across patients).

To find instantaneous speeds across time, the grid's instantaneous frequency first needed to be estimated. This was done by filtering from 7-13 Hz with a plateau-shaped filter with a transition width of 15%. A plateau-shaped filter was used instead of a more traditional Butterworth or FIR because the former isn't Gaussian in the frequency domain, and therefore does not bias the instantaneous frequency towards the center of the band-pass range[50]. The phase of the band-pass filtered data was then estimated using the angle of the Hilbert transform, and subsequently unwrapped. The first derivative of this phase series was defined as the difference in phase between consecutive samples, using MATLAB's diff function. Finally, to attenuate the sensitivity of this technique to noise, a median filter with a kernel of 10 samples was used[50].

Instantaneous speeds were calculated as follows: each channel's instantaneous frequency (see above paragraph) was divided by the magnitude of its phase gradient ($\sqrt{\nabla_x^2 + \nabla_y^2}$), yielding the instantaneous speed at each channel and timepoint. Then, at each timepoint, the median speed and frequency across all channels was found, and timepoints with a speed or frequency in the top or bottom .5th percentile was rejected to eliminate outliers. The distribution of these median speeds across time was then plotted as a normalized histogram (bin width of .01 m/s) for each patient and presented **Extended Data Fig. 3**. These normalized histograms were averaged and plotted in **Fig. 1c**.

To ensure that this effect was specific to the alpha-band, we re-applied our analysis techniques in a 1-5 Hz band and found that the significance of propagation (Rayleigh's Test for Non-Uniformity) was stronger in the alpha than delta band across all patients ($p = .0156$, Binomial Test).

Corticothalamic Interactions

Stereoencephalography (SEEG)[51] was performed on 9 patients to characterize epileptogenic activity and inform possible resections. SEEG probes were 2mm long and had 10-15 contacts with a .8mm diameter and 1.5mm inter-contact spacing. In Pts. 1-7, contact locations were found by stereotactic teleradiographs from within the stereotactic frame. These coordinates were then superimposed on a T1 MRI of the subject. An atlas[52] was then overlaid to determine the anatomical positions of thalamic and cortical contacts (**Fig. 2f**). Contacts were localized in Pts. 8-9 by aligning a post-operative CT with a pre-operative MRI. Adjacent channels (when at least one was in the grey matter) were referenced to each other to assure local generation of measured activity. Further use of contact, channel or site all refer to these bipolar channel pairs. Recordings were made at 256 Hz in Pts. 1-3, 128 Hz in Pts. 4-7 and 1024 Hz in Pts. 8-9. For further details see [53].

We analyzed spontaneous activity (36 ± 7.5 min., mean±standard deviation) during wakefulness prior to the onset of sleep, the time of which was determined behaviorally as well as electrographically by a qualified sleep-stager using standard methods[54]. The last three minutes of wakefulness before the onset of sleep was rejected to further avoid the analysis of sleep or excess drowsiness.

Prior to further analyses, we split the data into non-overlapping two-second epochs. We bandpass filtered (two-pass 3rd order Butterworth) thalamic activity in the alpha-band, then found the absolute value of its Hilbert transform to find single-trial thalamic alpha amplitude. Then, the 20% of epochs with the most total alpha-band amplitude (summing across thalamic bipolar pairs and samples) were used for further processing.

Cortical and thalamic power spectral peaks were found using the peakfinder[55] algorithm with a selectivity (the minimum difference a local maxima must have from its nearest minima to be considered a peak) of the power spectrum's range divided by 5. A channel was considered to have an alpha peak if it had at least one peak between 7-13 Hz.

To phase-align ongoing alpha activity (**Fig. 2d**), we picked the thalamic contact with the greatest alpha-band power and averaged the rest of our data (cortical and thalamic wide-band LFP and HGP) to alpha-band peaks in this channel. Alpha band peaks were found by bandpass filtering from 7-13 Hz (two-pass 3rd order Butterworth), taking the angle of the Hilbert Transform to find the phase, and then finding peaks in this series. LFP was high-pass filtered at 2 Hz (two-pass third-order Butterworth) prior to averaging on alpha peaks.

High-gamma-power (HGP) was derived by filtering from 70-120 Hz in Pts. 1-3 (due to a Nyquist frequency of 128 Hz) and 70-190 Hz in Pts. 8-9. The sampling rate in Pts. 4-7 (128 Hz) was too low to measure HGP. Although the former frequency band is somewhat lower than the usual definition of HGP (70-190 Hz), we observed similar results in subjects with both usual and reduced HGP bands (**Extended Data Fig. 6**). Furthermore, a previous study employing the same recordings demonstrated that 70-120 Hz HGP reliably decreased during K-complexes identical to 70-190 Hz power[53].

Granger Causality (GC) analyses were performed using the Multivariate Granger Causality Toolbox [21]. Frequency-resolved GC values were assessed between each corticothalamic channel pair in the non-overlapping 2-second epochs with the greatest 20% of thalamic alpha amplitude as found by the Hilbert Transform. In order to measure causality in the alpha-band without using a prohibitively large model-order, we then downsampled our data to 256 Hz and used a model order of 26 across all channels and patients (13 in patients with 128 Hz sampling rate). To ensure stationarity, we high-pass filtered at .2 Hz (Butterworth 2nd order two-pass) and then demeaned, detrended and z-scored each channel within each epoch. The lag needed for the autocovariance sequence of each epoch's vector auto-regressive model (VAR) to decay below the default numerical tolerance (10^{-8}) was computed with autocov_to_pwcgc(). Epochs which had an autocovariance lag of at least 2000 samples were deemed inappropriate for VAR modelling and were not used for Granger analysis.

Laminar Recordings

Laminar microelectrode arrays were inserted perpendicular to the cortical surface into tissue likely to be resected[56]. A silicone sheet attached to the array's top was used to keep the probe perpendicular to the cortical depth, with surface tension between the sheet and the pia, as well as pressure from the overlying grid and dura, keeping the array in place. This sheet also ensured that the laminar array was perpendicular to the cortex and that the first contact was placed just below the cortical surface (depth of ~175 microns in Pt.1 and ~150 microns in Pts. 2-3). Each laminar probe spanned the cortical depth with a length of 3.5 mm and diameter of .35

mm. Contacts had 40 micron diameters, spaced at 175 microns in Pt. 1 and 150 microns in Pt. 2-3. Recordings were made during 11.32 ± 0.48 min. (mean ± standard deviation) of quiet wakefulness.

The local-field-potential-gradient (LFPg), or the first derivative of the field potential (i.e. each contact referenced to its neighbor) and multi-unit activity (MUA) were recorded simultaneously at 2000 and 20000 Hz and filtered online from .2-500 Hz and 200-5000 Hz, respectively. Data from faulty channels (2 in each patient) were linearly interpolated from the channels directly above and below them.

Line noise was eliminated from both the LFPg and MUA by band-stop filtering (4 Hz bandwidth) at 60 Hz in Pt. 1-2 and 50 Hz in Pt. 3 (4th order Butterworth). The LFPg was then high-pass filtered at .5 Hz in Pts. 2-3 and 3.5 Hz in Pt. 1 due to a low-frequency vascular artifact (two-pass 2nd order Butterworth), HGP from 70-190 Hz and MUA from 300-3000 Hz (4th order Butterworth). MUA was then rectified and resampled at 2000 Hz. The data was then sub-sampled into two-second artifact-free epochs and, consistent with ECoG and SEEG, the 20% of epochs with the most alpha-band CSD amplitude across all channels was utilized for further analysis. In Pt. 1, all artifact-free epochs (not just those with the most alpha amplitude) were used due to a relatively short recording session. We observed no significant modulation of HGP or MUA in Pt. 1, probably due to technical concerns.

Current source density (CSD) was measured by taking the first spatial derivative of the LFPg (in effect the second spatial derivative of the monopolar field potential) and then applying a 5-point Hamming filter[22,57]. The Vaknin approximation (adding pseudo-channels of zeros to the LFPg above and below the array) was used to estimate the CSD on the second most deep and superficial channels of the laminar probe[58].

To visualize the profile of alpha CSD and HGP, we picked the laminar contact with the highest average alpha power, and averaged our HGP and CSD recordings to alpha-band peaks in the CSD of this channel. Alpha band peaks were found by bandpass filtering from 7-13 Hz (two-pass third-order Butterworth), taking the angle of the Hilbert Transform to find the phase, and then finding peaks in this series (corresponding to alpha-band current sinks). Average MUA displays were then smoothened with a Gaussian filter for display purposes (width of 5 ms and 750 microns, σ_x=10 ms and σ_y= 112.5 microns).

Prior to visualizing laminar power spectra as well as alpha power across channels (**Fig. 3g, h**), power spectra for each subject were normalized by dividing by the mean power from 4-25 Hz across all channels and epochs.

We localized laminar contacts to cortical layers by performing histology on explanted tissue in Pts. 1 and 3, and identifying a putative layer IV sink in Pt. 2 (**Supplementary Methods**)

Data Availability

We will make data and code available to the degree it is possible given participant consent restraints and HIPAA requirements. Macaque data is publically available at http://neurotycho.org/data/20120813ktanesthesiaandsleepchibitoruyanagawa.

Acknowledgements

The authors thank Erica Johnson, Nathan Meng, Richárd Fiáth, and Adam Niese for insightful comments, hypotheses and technical support. We also thank Project Tycho for making their macaque dataset publically available. This study was supported by the U.S. Office of Naval Research Grant N00014-13-1-0672, National Institutes of Health Grants R01-MH-099645, R01-EB-009282, R01-NS-062092, K24-NS-088568 and the MGH Executive Council on Research, Hungarian National Brain Research Program grant KTIA_13_NAP-A-IV/1- 4,6, EU FP7 600925 NeuroSeeker, and Hungarian Government grants KTIA-NAP 13-1- 2013-0001, OTKA PD101754, OTKA K119443.

Author Contributions

S.S.C. and I.U. conceived of the experiments; R.M.M, L.W., L.E., O.D., W.D., H.B., M.R., P.C., I.U., D.F., G.H., E.E, and S.S.C. conducted the experiments; M.H. analyzed the data; M.H., A.M. and S.S.C. interpreted the results; M.H., and S.S.C. wrote the manuscript, and all authors discussed and edited the manuscript.

Author Information

The authors declare no competing financial interests. Correspondence and requests for materials should be addressed to Milan Halgren (mhalgren@mgh.harvard.edu).